# Sputter-coated $TiO_2$ films as passivation and hole transfer layers for improved energy conversion with solar fuel $WO_3/CuWO_4$ photoanodes

Lucas C. Escaliante[a], Nilton Francelosi Azevedo Neto[b], Hervin Errol Mendoza[c], Chengcan Xiao[c], Rajesh Kandel[c], Jose Humberto Dias da Silva[a], Frank E. Osterloh[c]*

[a] *School of Sciences, Graduate Program in Materials Science and Technology – POSMAT, Universidade Estadual Paulista – UNESP. Avenida Engenheiro Luis Edmundo Carrijo Coube, 14-01, Bauru, São Paulo, 17033-360, Brazil.*

[b]*Plasma and processes laboratory, Instituto Tecnológico de Aeronáutica – ITA. Praça Marechal Eduardo Gomes, 50, São José dos Campos, São Paulo, 12228-900, Brazil*

[c] *Department of Chemistry, University of California, Davis. One Shields Avenue, Davis, California, 95616, United States of America.*

*Corresponding author: fosterloh@ucdavis.edu*

## ABSTRACT

Atomic layer deposited (ALD) "leaky" $TiO_2$ have gained interest as charge-selective protection layers for semiconductor solar fuel electrodes. Here we demonstrate the use of sputter-deposited $TiO_2$ layers as hole selective contacts for $WO_3/CuWO_4$ type 2 heterojunction water oxidation photoanodes for the first time. $TiO_2$ protection layers with varying thicknesses (2 to 128 nm) were deposited using the RF magnetron sputtering technique. The resulting $TiO_2$ films are amorphous based on Raman spectroscopy and powder XRD. Photoelectrochemical scans and Vibrating Kelvin probe photovoltage spectroscopy show that 2-8 nm $TiO_2$ layers nearly double the photocurrent to 0.97 mA $cm^{-2}$ under AM 1.5 illumination (19% AQE at 350 nm), increase the surface photovoltage signal by 25%, and increase the $WO_3/CuWO_4$ bandgap. These effects can be attributed to the

selectivity of $TiO_2$ for photoholes. Additionally, SPV data suggest that $TiO_2$ overlayers suppress copper-based surface recombination defects. Reduced photocurrent and the photovoltage are seen in thicker $TiO_2$ films (16 to 128 nm) as a result of an increasing hole transfer resistance and because of light shading effects according to photoaction spectra. The $TiO_2$ films also improve the stability of the $WO_3/CuWO_4$ photoelectrodes, allowing nearly constant $O_2$ evolution over 3 hours after an initial 20-35% loss. Overall, this work establishes RF magnetron sputtering as a useful method to install amorphous $TiO_2$ passivation layers for improved $WO_3/CuWO_4$ solar fuel photoelectrodes. Furthermore, we show how the combination of PEC with SPV measurements provides insight into the function of the $TiO_2$ coatings.

**Keywords:** Water splitting, RF magnetron sputtering, surface photovoltage spectroscopy, photoelectrochemistry, photoanode, $CuWO_4$, $WO_3$, $TiO_2$.

## INTRODUCTION

The water splitting (electrolysis) reaction[1,2] can generate carbon free fuels from sunlight and water. Photoelectrochemical (PEC) cells enable the process by combining photovoltage generation from a semiconductor with electrochemical water oxidation and reduction. Suitable photoelectrodes are stable against corrosion, have visible light active band gaps, high optical absorption coefficients, long charge carrier lifetime, fast charge transport, and do not utilize rare elements[3–6]. Bismuth vanadate fulfils several of these criteria, but its efficiency is constrained by its 2.4 eV band gap, which only allows 12% of the sunlight to be absorbed. $CuWO_4$ is a potential alternative due to smaller bandgap (2.2-2.4 eV)[7–10] combined with high stability in aqueous electrolytes[7,11,12]. Recently, it was shown that the photoanode performance of $CuWO_4$ can be improved by interfacing the material with $WO_3$. [13–17] The resulting type 2 heterojunction (**Figure 1a)** helps separate charge carriers and prevents them from recombination. $WO_3/CuWO_4$ heterojunction films can be made by various methods. Films grown by electrodeposition-annealing have shown to yield a water oxidation photocurrent of 0.80 mA/cm² at 1.23 V vs RHE[13], and films obtained by spin coating gave 0.5 mA/cm² at 1.23 V vs. RHE and 24% IPCE at 300 nm[18]. Sputtered / calcined $WO_3/CuWO_4$ films gave 0.35-0.45 mA/cm² at 1.23 V vs. RHE and an IPCE of 35% at 365 nm[16]. However, these values are still far away from the theoretical limit of $CuWO_4$. This may be attributed to intra-bandgap $Cu^{2+/+}$ surfaces states that reduce the carrier mobility and cause electron-hole recombination[9,10,19–21]. Additionally, these states may lead to Fermi level pinning resulting in a degraded junction and lower photovoltage[22,23]. These problems can potentially be overcome with $TiO_2$ overlayers. As was demonstrated recently, $TiO_2$ films prepared by Atomic Layer Deposition (ALD) can act as "leaky" protection layers[24,25] by allowing a hole current to pass through it via tunneling mechanism [2,26]. These layers also protect sensitive main group element

semiconductors from corrosion[2,24–31]. Accordingly, we speculate that $TiO_2$ layers can enhance the power conversion of $WO_3/CuWO_4$ photoanodes for oxygen evolution by forming a hole selective contact, as shown in **Figure 1b**.

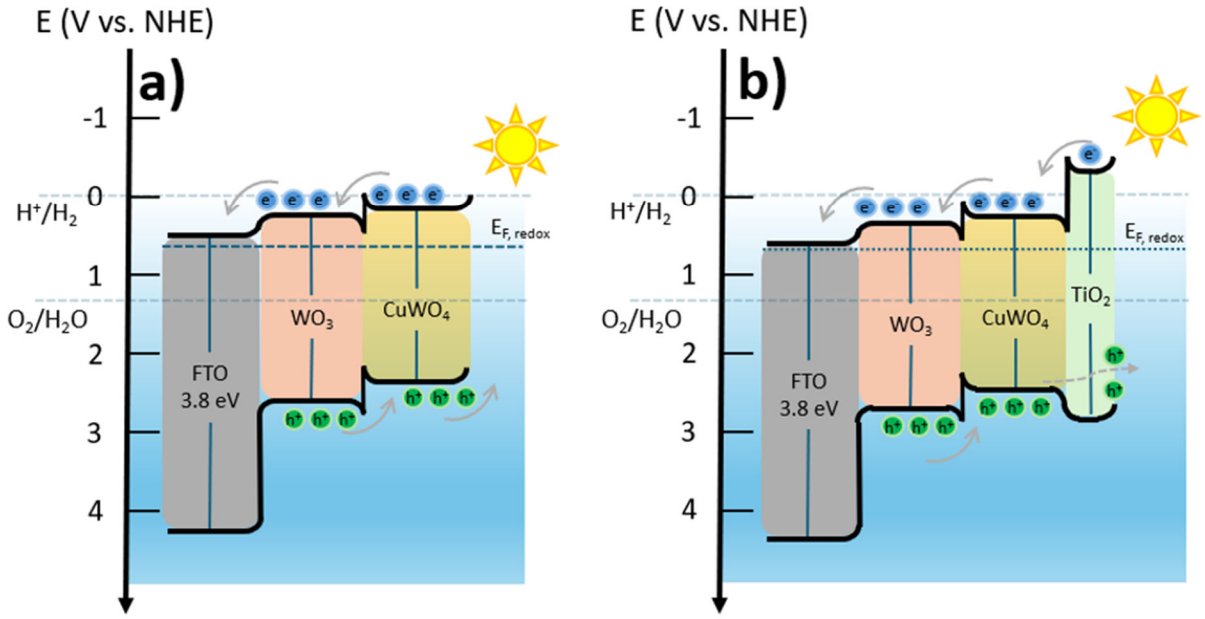


**Figure 1.** Band energy diagrams for a) FTO/$WO_3$/$CuWO_4$ and b) FTO/$WO_3$/$CuWO_4$/$TiO_2$ water oxidation photoanode, incl. depletion layers, Schottky barriers, ohmic back contacts, and charge carrier pathways.

To test this hypothesis, we grew $TiO_2$ layers onto $WO_3/CuWO_4$ photoanodes by RF magnetron sputtering deposition, similar to previous reports for Si photocathodes[32–35]. The resulting photoelectrodes are studied with a combination of X-ray diffraction, Raman spectroscopy, and electron microscopy, and further characterized with surface photovoltage spectroscopy, photoelectrochemical scans, photoaction spectra, and with oxygen evolution measurements. We find that the $TiO_2$ coatings do enhance the photoelectrochemistry of the

photoanodes by acting as hole selective contacts. However, in thick $TiO_2$ films these positive impacts are offset by light shading and by larger photohole transport resistance. To balance these influences requires optimization of the layer thickness, as described in the following.

## RESULTS AND DISCUSSION

The initial FTO/$WO_3$/$CuWO_4$ photoanodes of 1.0 cm² area size were obtained by magnetron co-sputtering from two targets about 10 cm away from the center of the substrate holder. The low-pressure chamber was evacuated and argon and oxygen were injected at 30 sccm and 10 sccm, respectively. A working pressure at 5 x $10^{-3}$ torr was used during the deposition, a working temperature of 500ºC, and a fixed RF electric power (180 W, 13.6 MHz) and DC power (10W) were applied to the W and Cu targets, respectively, for 2 hours. The sputtered films were then annealed in air (500ºC) to convert them into crystalline oxide films. This yields 1 μm thick films containing $WO_3$ and $CuWO_4$ phases in 1:1 ratio (submitted for publication). As we reported in the previous work, the activity of these films is enhanced by a type-2 heterojunction that separates photoelectrons towards $WO_3$ and photoholes towards $CuWO_4$ (**Figure 1**).

Next, $TiO_2$ surface layers of variable thickness were deposited by RF magnetron sputtering.[36] The depositions were conducted by applying 240 W of power on the RF source (Ti target) while flowing Ar and $O_2$ gases (flow rates of 40 and 2 sccm, respectively) at a 5 x $10^{-3}$ torr working pressure and at 250ºC. $TiO_2$ thickness was controlled via the deposition time (**Table S1**), after previous calibration on a control sample made by 8 h deposition[37](**Figure S1**). The thickness of the control sample was determined as 196 nm using the Cisneros[37] method, as described in the supporting information (**Equations S1-4**). Shorter deposition times yield $WO_3$/$CuWO_4$/$TiO_2$ – d

samples where the thickness d is 2 nm, 4 nm, 8 nm, 16 nm, 48 nm, 96 nm, and 128 nm. Powder XRD data of the $WO_3/CuWO_4$ samples is summarized in **Figure 2**. Before $TiO_2$ addition, many of the main diffraction peaks of $CuWO_4$ (JCPDS 88-0269) are observed, in addition to several $WO_3$ peaks (JCPDS 71-0305), for example, (0 2 2), (0 -2 2), (2 0 2), (2 2 2), (-1 4 0), and (-1 1 4) and a few FTO diffraction peaks (JCPDS 71-0625). Some peaks from $CuWO_4$ and $WO_3$ are found to overlap with each other. For example, the $CuWO_4$ peaks (1 1 0), (0 -1 1), and (0 1 1) and $WO_3$ peaks (0 0 2), (0 2 0), and (2 0 0) have the same diffraction angle. Based on a Rietveld refinement ($R_{wp}$ = 17.769), the phase composition of the sample is 61.9% $CuWO_4$: 38.1% $WO_3$.

**Figure 2** also gives the diffraction pattern of a 128 nm $TiO_2$ reference film grown on a $SiO_2$ substrate. On the $SiO_2$ substrate, peaks for rutile and anatase $TiO_2$ (JCPDS 72-1148 and JCPDS 71-1166, respectively), can be identified clearly. Interestingly, these peaks are completely absent in the FTO/$CuWO_4$/$WO_3$/ $TiO_2$ – 128 nm sample. This shows that the $TiO_2$ film on top of $WO_3/CuWO_4$ is amorphous.

In order to further investigate the chemical composition of the films, Raman spectroscopy was employed. Spectra for $SiO_2/TiO_2$, FTO/$WO_3$/$CuWO_4$, and FTO/$WO_3$/$CuWO_4$/$TiO_2$ – 128 nm are summarized in **Figure 3**.

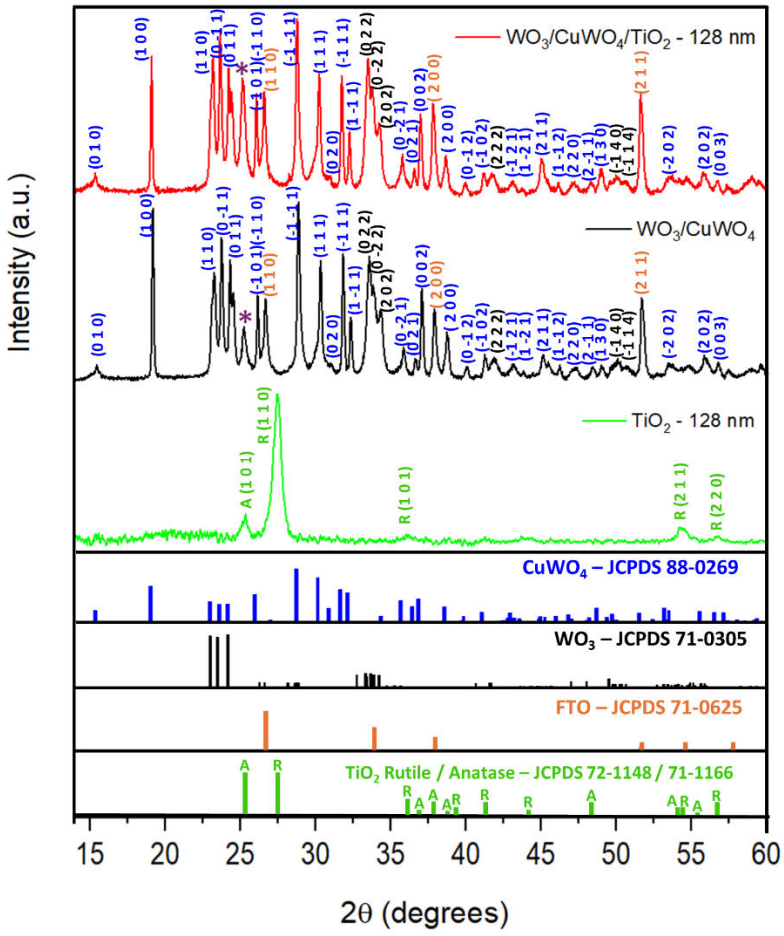


**Figure 2**. Powder XRD data (Cu-Kα, 1.54056 Å) for $CuWO_4/WO_3$, $CuWO_4/WO_3/TiO_2$ - 128 nm, and for $TiO_2$ grown on $SiO_2$. Reference patterns are shown also.

Out of 18 active vibrational modes of $CuWO_4$, 14 are observed in $FTO/WO_3/CuWO_4$ and $FTO/WO_3/CuWO_4/TiO_2$ – 128 nm[38–40], and 3 of the vibrational modes of $WO_3$[41,42] . Again, whereas a $TiO_2$ film grown on $SiO_2$ shows 4 vibrational modes related to the Rutile, Anatase, and Brookite phases of the $TiO_2$[36], no vibrational modes belonging to $TiO_2$ are seen for $WO_3/CuWO_4/TiO_2$ – 128 nm. This data suggests that $TiO_2$ layers deposited onto $WO_3/CuWO_4$

heterostructures are amorphous while similar $TiO_2$ layers deposited onto $SiO_2$ are crystalline. The amorphization on $WO_3/CuWO_4$ deposited $TiO_2$ is attributed due to the complex interface between $WO_3$ and $CuWO_4$, which induces localized strain, distortions in the $TiO_2$ lattice, and structural disorder. Amorphization does not occur on $SiO_2$ crystals due to the smooth surface which allows the $TiO_2$ to crystallize more freely.

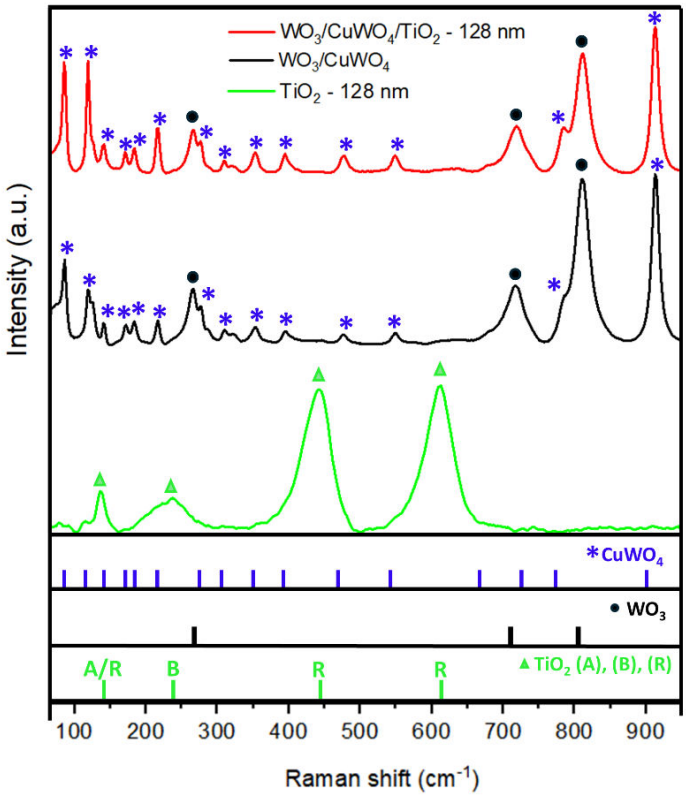


**Figure 3**. Raman spectra of the samples and the corresponding reference spectra. A, B, and R labels identify Anatase, Brookite, and Rutile vibrational modes, respectively.

To determine the effect of the $TiO_2$ coating on the sample morphologies and chemical composition, scanning electron microscopy (SEM) measurements coupled with Energy Dispersive Spectroscopy (EDS) were performed. As can be seen in **Figure 4**, the FTO/$WO_3$/$CuWO_4$ film contains grains and pores on the 200 - 400 nm scale, without any discernible facets. According to EDS, the film is composed of 64.9 (atom)% of oxygen, 23.3(atom)% of tungsten, and 11.8(atom)% of copper (**Figure S2**). This corresponds to a 60.7: 39.3% ratio of $CuWO_4$ and $WO_3$, which is in excellent agreement with the composition suggested by the Rietveld refinement ($CuWO_4$:$WO_3$ = 61.9% :38.1%). In comparison, the FTO/$WO_3$/$CuWO_4$/$TiO_2$ – 128 nm sample in **Figure 4b** has an elemental composition of 64.1(atom)% O, 17.9(atom)% W, 9.3(atom)% Ti, and 8.8(atom)% Cu (**Figure S3**) and shows a homogeneous distribution of Ti. This confirms the presence of a conformal $TiO_2$ overlayer. This overlayer is also responsible for the lower image contrast in the SEM.

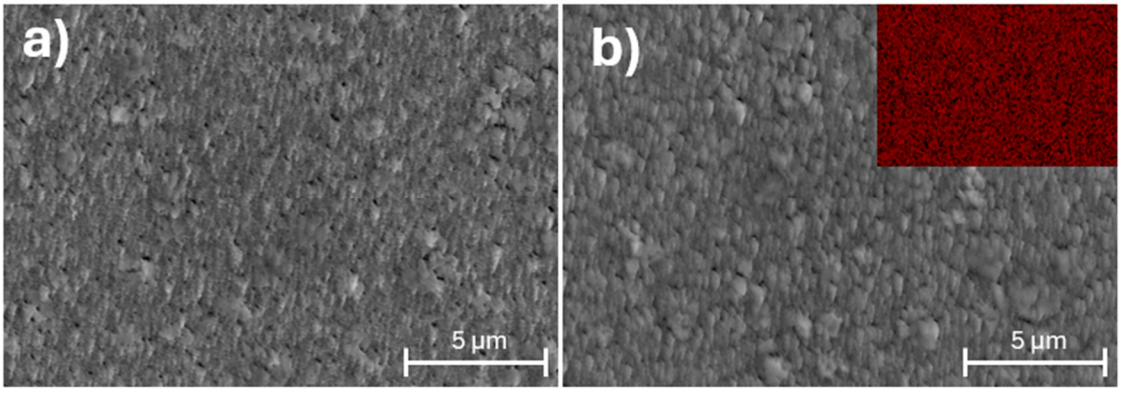


**Figure 4.** SEM images for a) FTO/$WO_3$/$CuWO_4$ and b) FTO/$WO_3$/$CuWO_4$/$TiO_2$ – 128 nm at 10,000x magnification. The insert shows the Ti distribution (red color) from EDS.

Photos of the films are given in **Figure 5.** The yellow appearance is expected for $WO_3/CuWO_4$, which absorbs light only in the blue part of the visible spectrum. There are no visible changes resulting from the addition of the $TiO_2$.

Diffuse reflectance optical absorbance spectra for all samples are shown in **Figure 6**. The FTO/$WO_3/CuWO_4$ sample has an absorption edge at 531 nm (2.33 eV) near the tabulated band gap of $CuWO_4$ (2.2-2.4 eV). Addition of thin (2-8 nm) $TiO_2$ layers moves the absorption edge to slightly higher wavelength (543 nm, 2.28 eV), while thicker $TiO_2$ films (16-128 nm) diminish the *apparent* absorption below 500 nm. These optical changes arise from interference between light beams reflected at the front and back of the $TiO_2$ films[43,44], which modifies the diffusely reflected signal. These refractive properties [45,46] are the basis for the thickness determination of the deposited $TiO_2$ films, [37] as shown in **Figures S1 and S4**. However, the interference effect makes it difficult to determine the band gap of the $TiO_2$ coated films from optical spectra.

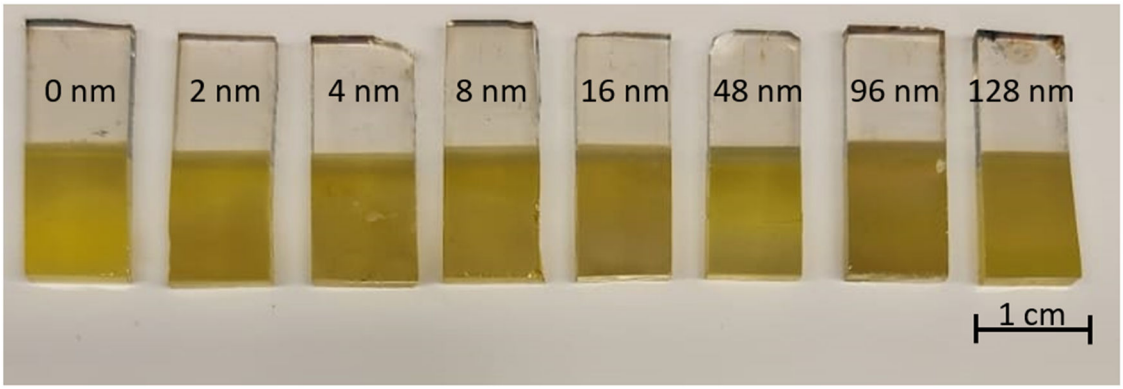


**Figure 5.** Photos of $WO_3/CuWO_4$ films on FTO with variable $TiO_2$ overlayers (thickness as labelled).

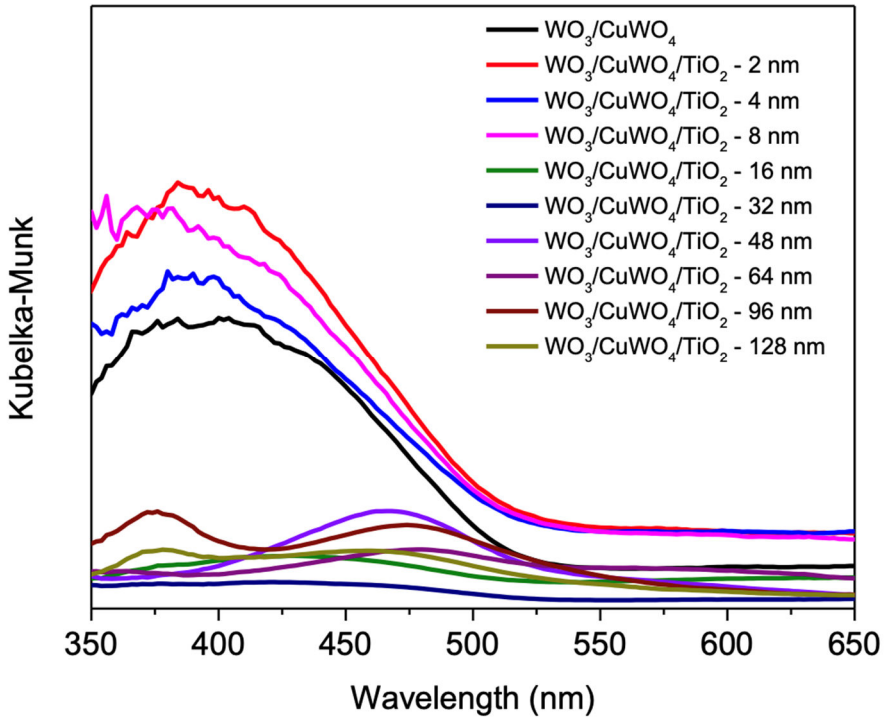


**Figure 6.** Diffuse Reflectance Optical Spectra for samples shown in **Figure 5**. The absorbance variations at <500 nm are attributed to optical interference effects at the new $TiO_2$-air interface[45,46]. See also **Figures S1 and S4**.

To complement the optical spectra and to observe the contribution of the $TiO_2$ overlayer to the photovoltage of the FTO/$WO_3$/$CuWO_4$ samples, vibrating Kelvin probe surface photovoltage spectroscopy (SPS) was employed. In this method, the contact potential difference (CPD) of the sample relative to the gold reference electrode is measured with a semi-transparent gold Kelvin probe[47]. The change CPD in going from dark to illumination defines the surface photovoltage signal, SPV = CPD (light) – CPD (dark)[48–50]. For conductive samples, the SPV equals the photovoltage, i.e. the electric potential difference between majority and minority charge carriers at the interfaces[50–52]. Spectra for all films are shown in **Figure 7a**.

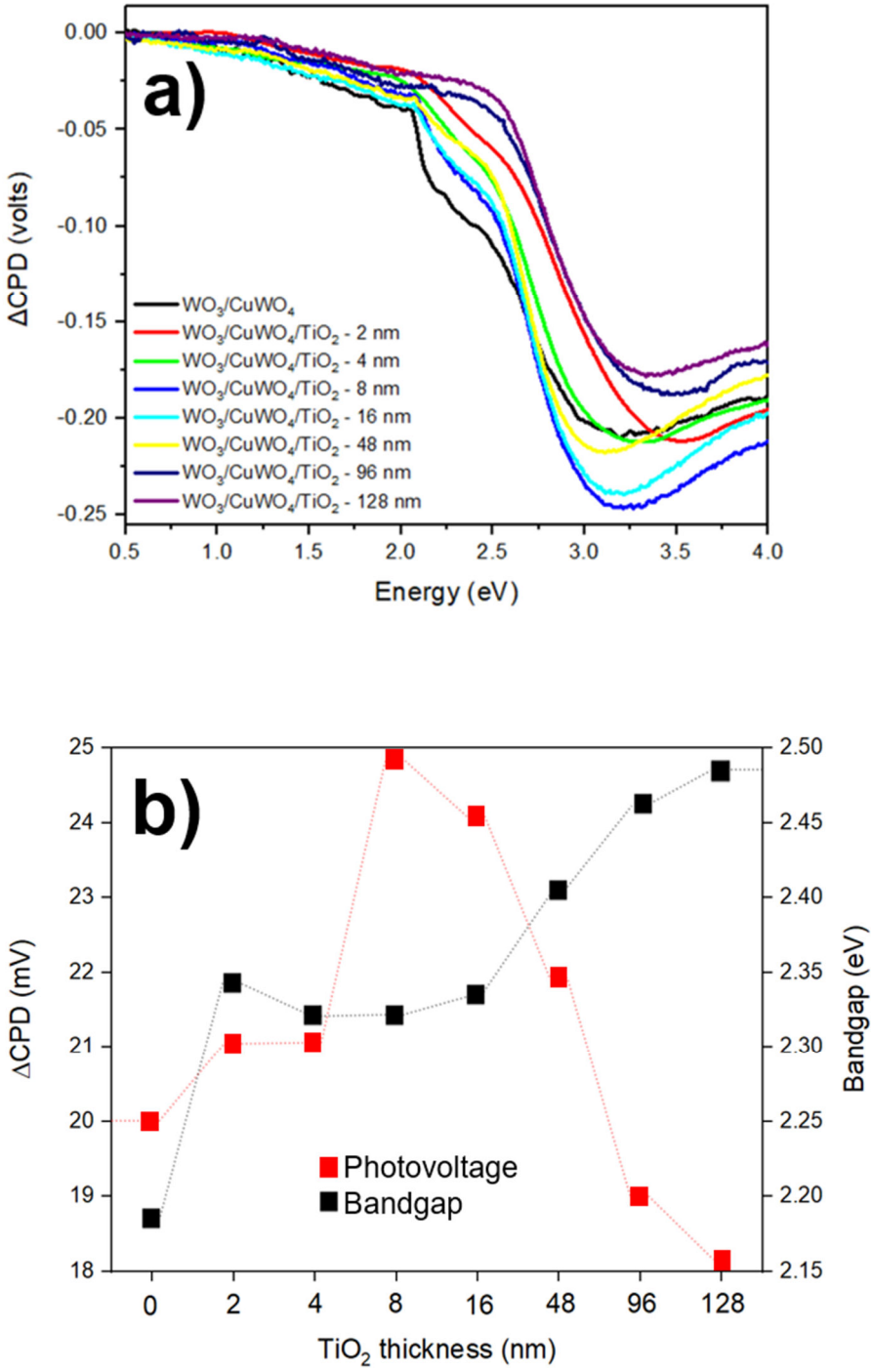


**Figure 7.** a) Surface Photovoltage Spectroscopy. b) Correlation between $TiO_2$ thickness and effective SPS bandgap.

All have negative SPV signals, indicative of photoholes moving towards the Kelvin probe as shown in **Figure 8a**. This is typical for n-type semiconductors[53], where electrons are repelled by the electric barrier of an electron depletion layer at the surface. Tangential fitting of the major SPV signal to the baseline yields the *effective band gap* of each film. These values are summarized in **Table 1** and plotted in **Figure 7b** together with the maximum SPV signals. The SPV signal shows a volcano-like trend: It increases for thin $TiO_2$ coatings (2, 4, 8 nm) and then decreases for thicker $TiO_2$ films. Possible reasons for the SPV decrease are light shading from $TiO_2$ caused by parasitic absorption and refraction of light, [43,44] as suggested by the optical spectra in **Figure 6**. Additionally, an increased hole transfer resistance by the thicker $TiO_2$ films may be responsible for the SPV decrease[2,24–26].

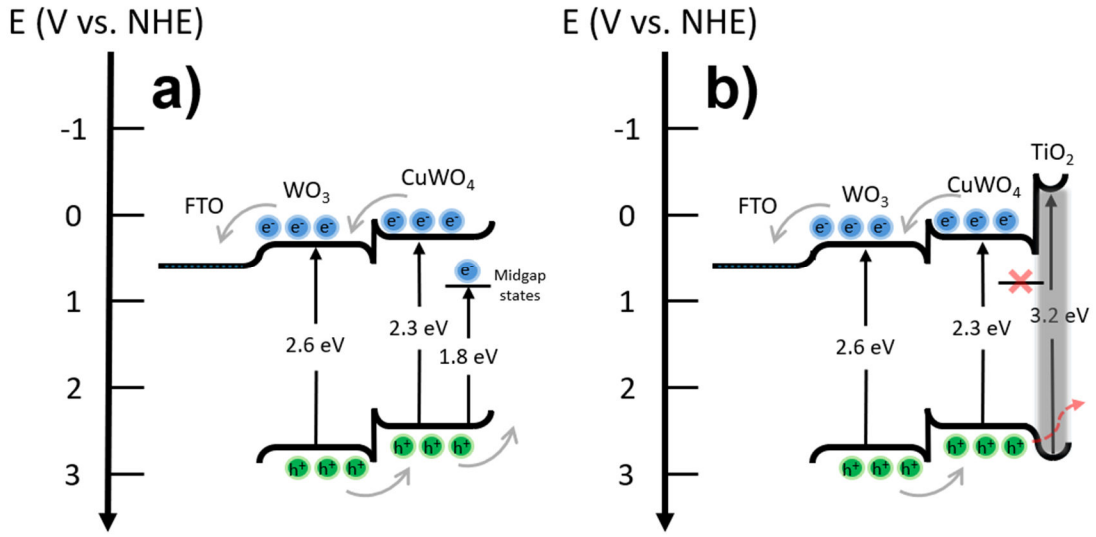


**Figure 8.** Photochemical charge transfer producing the SPV signal in a) $WO_3/CuWO_4$, and b) $WO_3/CuWO_4/TiO_2$ films. In b), the $TiO_2$ passivating layer removes the mid gap state but also introduces a hole transfer resistance (red arrow).

**Table 1.** Photovoltage, SPS bandgaps, photocurrent, photo-onset, and Faraday efficiency for $WO_3/CuWO_4$ samples with and without $TiO_2$.

| **Sample ($TiO_2$ thickness /nm)** | **0** | **2** | **4** | **8** | **16** | **48** | **96** | **128** |
|---|---|---|---|---|---|---|---|---|
| **ΔCPD (mV)** | 20 | 21 | 21 | 25 | 24 | 22 | 19 | 18 |
| **Effective Bandgap (eV)** | 2.18 | 2.34 | 2.32 | 2.32 | 2.33 | 2.40 | 2.46 | 2.48 |
| **Photocurrent ($mA/cm^2$)** | 0.51 | 0.96 | 0.97 | 0.90 | 0.75 | 0.60 | 0.33 | 0.24 |
| **Photocurrent onset (V vs. RHE)** | 0.53 | 0.57 | 0.57 | 0.59 | 0.58 | 0.61 | 0.62 | 0.61 |
| **Faraday Efficiency (%)** | 96 | 97 | 98 | 79 | 67 | 73 | 100 | 43 |

As **Figure 7b** shows, effective band gap values increase from 2.18 eV for the non-modified $WO_3/CuWO_4$ film to 2.48 eV for the sample with the thickest (128 nm) $TiO_2$ film. The trend has a discontinuity for films with 2 and 4 nm thickness, which have higher than expected effective band gaps. This is attributed to the removal (passivation) of surface defects by the $TiO_2$ films as shown in **Figure 8a** and **b**. Such defects consisting of $Cu^{2+/+}$ states were previously identified on the basis

of SPV and photoelectrochemistry studies[10,54]. The $Cu^{2+/+}$ state is 1.8 eV (690 nm) above the $CuWO_4$ valence band allowing direct excitation of electrons into it[10]. These states are quenched upon coating with 2-8 nm $TiO_2$. The raises the photoonset to 2.3 eV, which is identical to our previously reported band gap value for $CuWO_4$[10]. Additionally, the effective bandgap increase for the thicker $TiO_2$ films may result from the increasing photohole transfer resistance of $TiO_2$ (red arrow in **Figure 8b)**. Overcoming this resistance in the thicker films requires photons of progressively higher energy. A similar effect was demonstrated by Tilley's group for ALD grown $TiO_2$ on a variety of semiconductors[25]. This hole transfer resistance is also responsible for the reduction of the maximum photovoltage signal in samples coated with >8 nm $TiO_2$. Overall, these experiments reveal the passivating and hole transfer limiting effects of $TiO_2$ coatings on the photovoltaic behavior of the FTO/$WO_3$/$CuWO_4$/$TiO_2$ films.

Next, to determine the ability of the films to convert solar energy into fuel, photoelectrochemical scans under AM 1.5 illumination were recorded in an aqueous phosphate buffer solution at pH 6.5, as shown in **Figure 9**. All samples produce anodic photocurrents that can be attributed to water oxidation and oxygen evolution (see below). The anodic photocurrent begins at potentials of 0.53 V RHE for the FTO/$WO_3$/$CuWO_4$ electrode and reaches up to 1.0 mA $cm^{-2}$ at 1.23 V RHE for the FTO/$WO_3$/$CuWO_4$/$TiO_2$ - 4 nm sample, almost twice the value of the non-$TiO_2$ coated sample. The other samples produce intermediate photocurrents (**Table 1** and **Figure 9**), which decrease monotonically with $TiO_2$ thickness. This trend mimics the photovoltage behavior in **Figure 7b**. It can be attributed to a hole transfer resistance of the $TiO_2$ coating. This explains the photocurrent decay seen in **Figure 9c**.

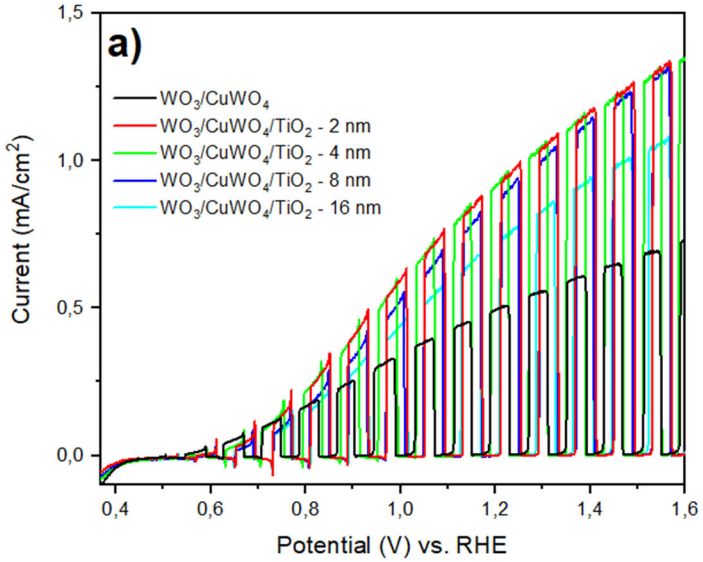
a)
WO3/CuWO4
WO3/CuWO4/TiO2 - 2 nm
WO3/CuWO4/TiO2 - 4 nm
WO3/CuWO4/TiO2 - 8 nm
WO3/CuWO4/TiO2 - 16 nm
Current (mA/cm2)
Potential (V) vs. RHE
1,5
1,0
0,5
0,0
0,4
0,6
0,8
1,0
1,2
1,4
1,6

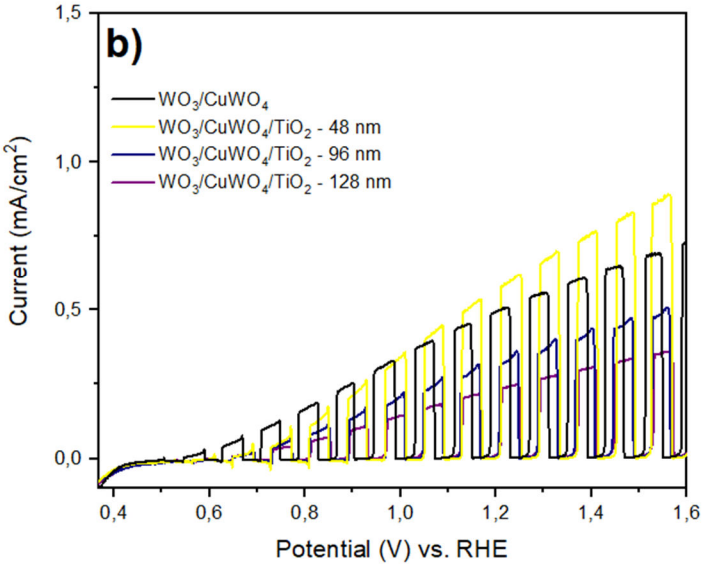
b)
WO3/CuWO4
WO3/CuWO4/TiO2 - 48 nm
WO3/CuWO4/TiO2 - 96 nm
WO3/CuWO4/TiO2 - 128 nm
Current (mA/cm2)
Potential (V) vs. RHE
1,5
1,0
0,5
0,0
0,4
0,6
0,8
1,0
1,2
1,4
1,6

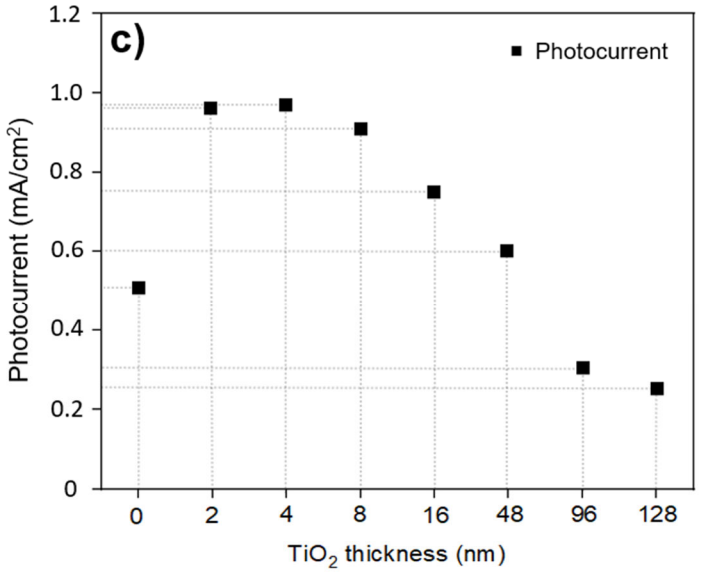


**Figure 9.** Linear sweep voltammograms in a 0.1 M phosphate buffer solution at pH 6.5 under AM 1.5 G irradiation from a 300 W xenon arc lamp. (a) $WO_3/CuWO_4$, $WO_3/CuWO_4/TiO_2$ – 2 -16 nm, (b) for $WO_3/CuWO_4$, $WO_3/CuWO_4/TiO_2$ – 48 - 128 nm. (c) Photocurrent (1.23 V RHE) comparison.

Additionally, the $TiO_2$ layer causes small change in the photocurrent onset potential (photovoltage). While FTO/$WO_3/CuWO_4$ has an onset of 0.53 V vs. RHE (**Figure 9a**), corresponding to a photovoltage of 1.23 V - 0.53 V= 0.70 V, samples with added $TiO_2$ have onsets between 0.57 and 0.62 V vs. RHE, and correspondingly lower photovoltage. The photovoltage loss increases with $TiO_2$ thickness, and therefore is ascribed to the hole transfer resistance of $TiO_2$. As holes accumulate near the $CuWO_4/TiO_2$ interface, the positive charge moves the $WO_3/CuWO_4$ Fermi levels to more oxidizing values.

To complement the SPS and photoelectrochemical scans, photoaction spectra were recorded for all samples (**Figure 10**). As expected, incident photon to current conversion efficiency (IPCE) values vary strongly with photon energy. Non-zero IPCE values are observed at photon

energies above the band gap of $CuWO_4/WO_3$. The highest IPCE occurs at 350 nm for samples with 2 – 16 nm $TiO_2$ (**Figure 10a**), and at 400 nm for samples with 48 - 128 nm $TiO_2$ overlayers. Below 400 nm, IPCE values decline sharply. This is due to the shorter light penetration depth at these wavelength. Because excitation only occurs in the front 100~150 nm of each sample, electron transport to the back electrode becomes a limiting factor. Samples coated with 48 - 128 nm $TiO_2$ experience shading form parasitic light absorption from $TiO_2$ ($E_G$ 3.0 eV). This explains the lower 350 nm IPCE values for these samples. Additionally, the data shows that samples coated with 2-16 nm $TiO_2$ layers have 50% higher IPCE values (15.0%, 15.7%, 19.0%, and 11.3%, respectively at 350 nm) than the bare FTO/$CuWO_4/WO_3$ sample (9.3%). This agrees with the SPV and photoelectrochemistry data above. It reflects the suppression of the $Cu^{2+}$ recombination by thin $TiO_2$ layers and the insulating effect of thick $TiO_2$ overlayers on photohole transport to the electrolyte. These two opposing influences are best balanced for the 8 nm $TiO_2$ overlayer, allowing the highest IPCE in that case (**Figure 10c**).

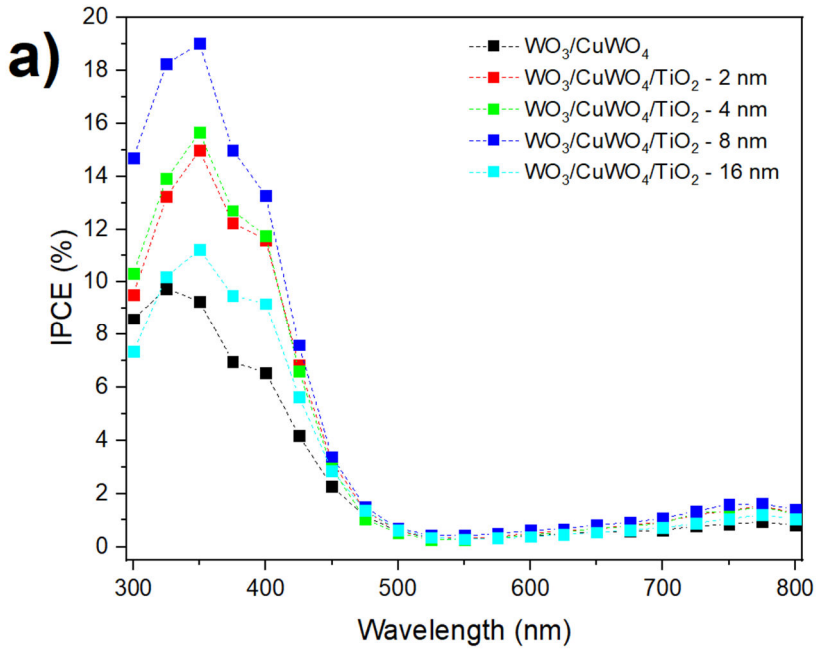

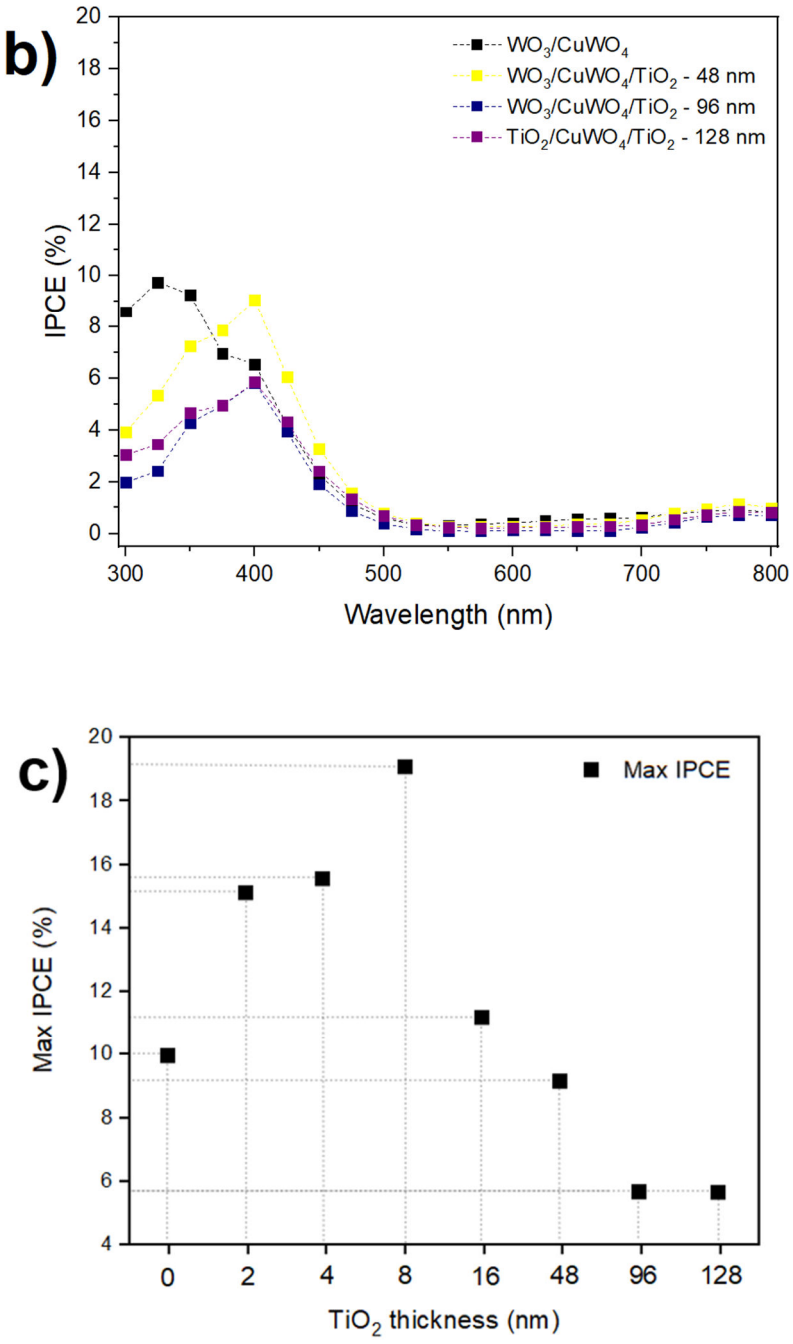


**Figure 10.** Photoaction spectra for $WO_3/CuWO_4/TiO_2$ electrodes in 0.1 M phosphate buffer solution at pH 6.5. a) Samples with 0, 2, 4, 8, and 16 nm of $TiO_2$. b) Samples with 48, 96, and 128 nm of $TiO_2$. c) Comparison of max IPCE values. Non-zero IPCE values at $\lambda$>550 nm are a measurement artefact resulting from second order diffraction at the monochromator optical grating. See optical emission spectra in **Figure S5**.

Lastly, chronoamperometry and Faraday efficiency measurements were performed to assess the stability of the samples and their ability to generate $O_2$. According to **Figure 11** almost all samples loose 20-35% of their photocurrent in the first 20 mins under ~ 5 suns illumination, but then remain relatively stable (~90% of current maintained) for 180 minutes. Based on the literature, $WO_3/CuWO_4$ electrodes are regarded stable under 1 sun illumination in neutral aqueous solutions[12,17,55]. Stability is maintained with the $TiO_2$ coatings and improved for $WO_3/CuWO_4/TiO_2$ – 8, 16, 48 nm.

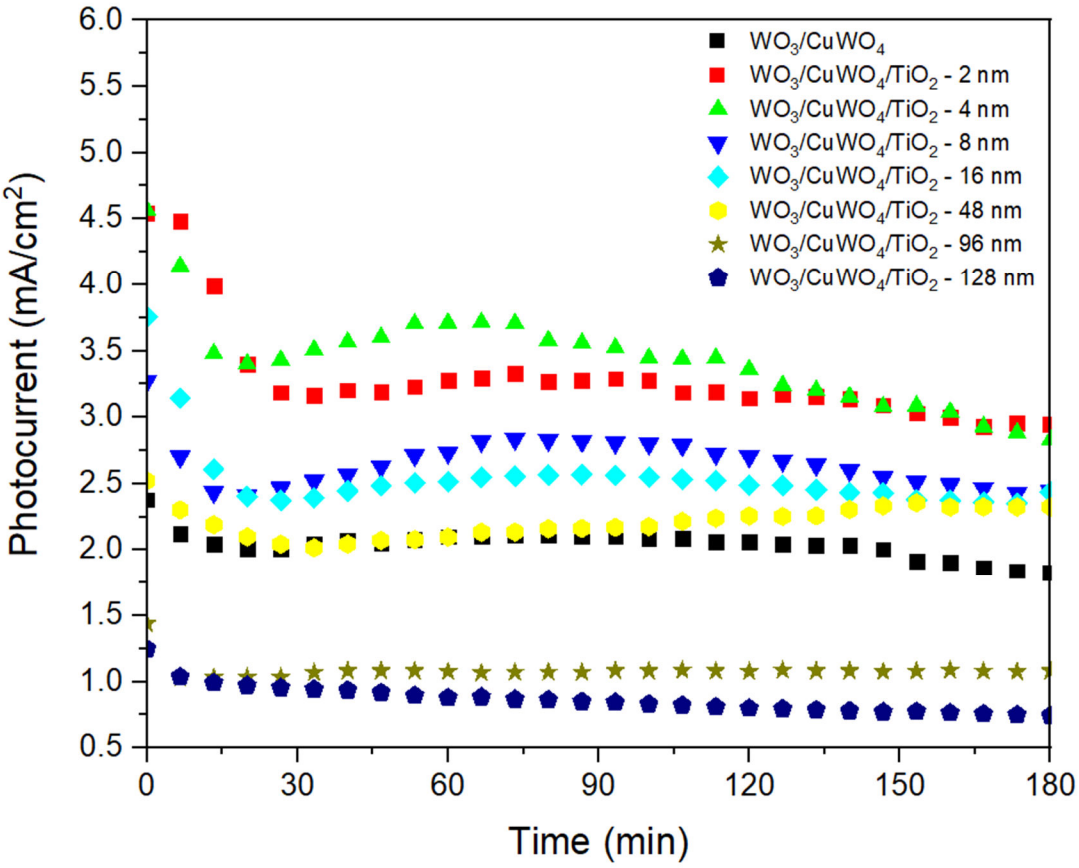


**Figure 11.** Photocurrent at 1.23 V vs. RHE in 0.1 M phosphate buffer solution at pH 6.5 under 464-496 mW cm$^{-2}$ illumination from a 300 W xenon arc lamp. The higher light intensity was chosen to specifically probe the aging of the electrodes.

**Figure 12** shows $O_2$ generated with each photoelectrode over the 3 h illumination experiment. Oxygen concentrations rise nearly linearly, with rates determined by the photocurrent of each electrode. Calculated Faraday efficiencies are presented in **Table 1**. Near unity values are seen for $WO_3/CuWO_4/TiO_2$ – 0, 2, and 4 nm, while values near 75% occur for films with thicker $TiO_2$ films. This suggests that other oxidation processes are contributing to the photocurrent in these cases. Indeed, $TiO_2$ photoanodes have been reported to generate $H_2O_2$ in addition to $O_2$[56–58]. However, a preliminary analysis via iodometry (oxidation of potassium iodide) did not detect any $H_2O_2$. Further studies are needed to determine the cause of the lower Faraday efficiency.

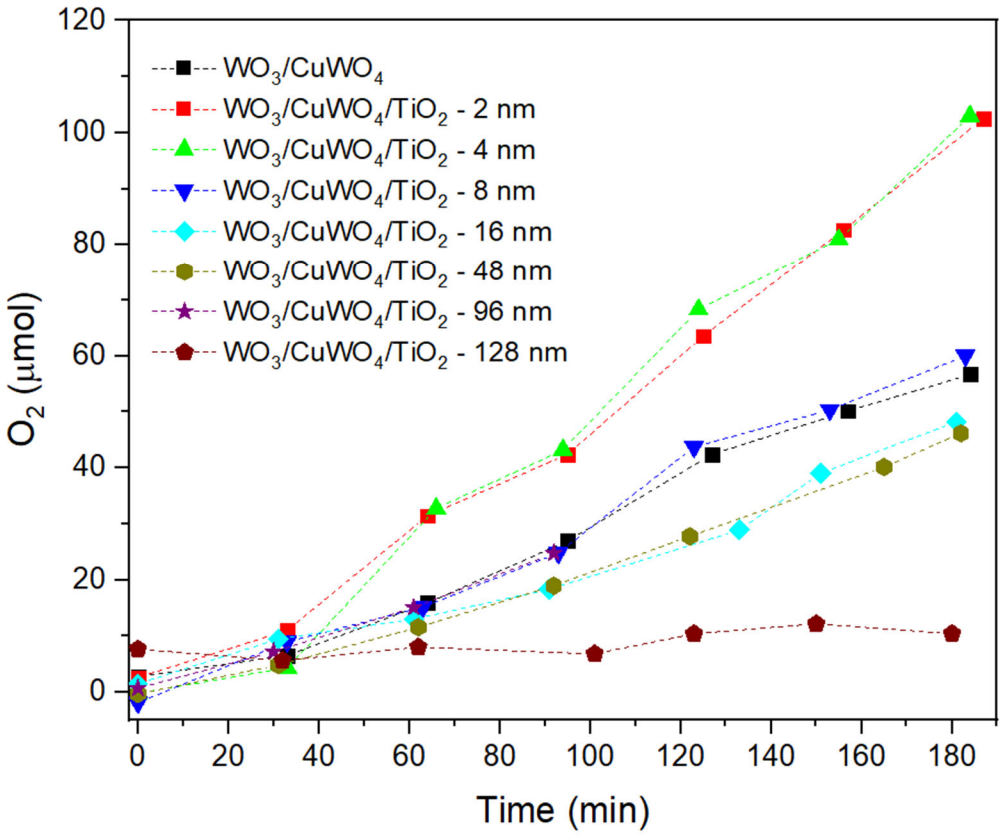


**Figure 12.** Oxygen evolution for $WO_3/CuWO_4$ and $WO_3/CuWO_4/TiO_2$ electrodes at 1.23 V vs RHE in 0.1 M phosphate buffer solution at pH 6.5 under ~500 $mWcm^{-2}$ illumination from a 300 W xenon arc lamp.

## CONCLUSIONS

FTO/$WO_3$/$CuWO_4$/$TiO_2$ electrodes with enhanced photoelectrochemical water oxidation properties were achieved by the addition of sputtered $TiO_2$ overlayers for the first time. According to XRD diffraction, Raman spectroscopy, and SEM / EDS measurements, the $TiO_2$ overlayers are amorphous and have thickness between 2 and 128 nm. Thin (2 - 8 nm) $TiO_2$ layers increase the photocurrent and the photovoltage, according to photoelectrochemical scans and vibrating Kelvin probe surface photovoltage spectroscopy. This is attributed to improved charge separation at the $TiO_2$ hole selective contact. Additionally, SPV data suggests that $TiO_2$ passivates $WO_3$/$CuWO_4$ surface defects and increases the effective band gap of the $WO_3$/$CuWO_4$ composite. With thicker $TiO_2$ coatings (16 – 128 nm) these benefits are offset by an increased hole transfer resistance and a shading effect from $TiO_2$. $TiO_2$ coatings also mildly increase the stability of the $WO_3$/$CuWO_4$ photoelectrodes during 3 hour experiments under 5 sun illumination, but result in lower $O_2$ evolution Faraday efficiencies, for reasons not entirely clear. Overall, this work establishes sputter coating of amorphous $TiO_2$ as a method to enhance the water oxidation performance of $WO_3$/$CuWO_4$ solar fuel photoelectrodes. We expect that these results can be applied to other metal oxide photoanodes.

## EXPERIMENTAL

**Synthesis.** Reactive RF and DC magnetron sputtering was performed in a commercial Kurt J. Lesker reactor using Macashew Tungsten (99,999%) and Kurt J. Lesker copper (99.99%) targets. $WO_3/CuWO_4$ films were first deposited onto FTO/glass substrates from MSE supplies (15 Ω/sq), as described in our previous publication (submitted for publication). $TiO_2$ depositions were conducted by applying 240 W RF power on the Ti target while flowing Ar and $O_2$ gases at flow rates of 40 and 2 sccm, respectively, and using 5 x $10^{-3}$ torr total pressure. The temperature during the deposition was controlled by a Neocera heater/controller adjusted to 250ºC. The real temperature measured by an attached thin cromel-alumel thermocouple was 150 ± 20°C. The difference is due to heat losses in the heater-substrate interface and the chamber walls which remain at room temperature.

**Characterization.** The structural properties of the films were analyzed by X-ray diffractometry in a Rigaku D-Max – 2100/PC equipment, with Cu Kα (1.54056 Å) radiation, and using a Bruker D8 Advance Eco with Cu Kα and a monochromatic wavelength of 1.5418Å, using 2θ configuration, 15-60º range, and a step size of 0.01º. Raman spectroscopy (Horiba-Evolution) analysis was performed in a spectral resolution lower than 1 $cm^{-1}$ with a 532 nm laser to evaluate the vibrational modes of the samples. The morphology of the samples was observed with an FEI Scios Dual Beam FIB/SEM microscope (scanning electron microscopy) with Oxford X-Max Energy Dispersive X-ray Spectroscopy (EDS) Detector and accelerating voltage of 10-20 KV. The optical properties of the samples were verified with measurements on a Perkin Elmer *Lambda 1050* UV/Vis/Nir spectrophotometer (data interval of 1.00 nm) at a scan speed of 141 nm/min. Surface photovoltage spectroscopy was performed in air environment utilizing a semi-transparent vibrating gold-mesh

Kelvin probe (Delta PHI Besocke) controlled by a Kelvin Control 7 Oscillator/amplifier (Besocke Delta Phi). Samples were illuminated through the Kelvin probe with monochromatic light in the 3390−40,000 $cm^{-1}$ range generated by an Oriel Cornerstone 130 monochromator powered by a 300 W Xe arc lamp source. The light intensity at the sample was 50-150 $\mu W/cm^2$. Spectra were acquired by stepping the photon energy by 0.0124 eV every 5 seconds and by measuring the contact potential difference (CPD) value at each step. The SPV signal was obtained according to SPV=CPD(light)-CPD(dark). Before each scan, a stable CPD baseline was first established.

Electrochemical characterizations were performed using a Gamry Reference 600 Potentiostat linked to a photoelectrochemical cell (PEC), filled with 50 mL of 0.1 M $Na_2HPO_4/NaH_2PO_4$ buffer solution at pH 6.5, and containing a Pt counter electrode and a saturated calomel reference electrode separated by a KCl salt bridge. The cell was open to air and constantly stirred at 300 rpm. Chopped light linear sweep voltammetry measurements were performed under AM 1.5 G irradiation from a 300 W xenon lamp source. The irradiance at the electrode was 100 mW $cm^{-2}$, as determined by calibration with via commercial silicon solar cell. The system was also calibrated using the redox potential $K_4[Fe(CN)_6]$ at 0.358 V (NHE). IPCE measurements were performed at 1.23 V vs RHE using light from an Instruments SA, Inc. H10 1200 (350-800 nm) monochromator behind a 300 W Xenon lamp. The wavelength was reduced in 25 nm increments beginning at 875 nm. The irradiance at each wavelength was measured using a NIST Traceable radiometer/photometer from *International Light*, and the IPCE values were calculated using equation 1 below. Here, $j_{ph}$ is the photocurrent density in $mA/cm^2$ at 1.23 V RHE, h is the Planck's constant ($6.62\times10^{-34}$ J·s), c is the speed of light ($3.0\times10^{8}$ m/s), e is the charge of a single electron ($1.6\times10^{-19}$ C), $P_{mono}$ is the power density of monochromatic light in $mW\cdot cm^2$, and $\lambda$ is the monochromatic wavelength of light in nm.

$$IPCE = \frac{j_{ph}\, x\, \frac{hc}{e}}{P_{mono}\, x\, \lambda} \times 100\% \quad (1)$$

For Faraday efficiency measurements, two salt bridges were used (one of them containing the Pt counterelectrode open to air). The cell was sealed to avoid air contamination, and the cell was purged with argon for 20 min prior to the experiment. Chronoamperometry was performed at 1.23 V vs RHE for 180 minutes. 50 μL of gas was collected from inside of the cell every 30 min and injected into a Varian CP-3800 gas chromatograph to measure the amount of oxygen. Equation 2 was used to calculate the theoretical amount of oxygen. Here, Q is the charge in Coulomb ($\int_0^t Idt$), n is the number of electrons, and F is the Faraday constant 96,485 C/mol.

$$O_2,\ theory = \frac{Q}{n.F} = \frac{\int_0^t Idt}{4\,.\,96485} \quad (2)$$

**ACKNOWLEDGMENT**

The authors thank the Fundação de Amparo à Pesquisa do Estados de São Paulo – FAPESP for financial support via grants 2022/06542-9 and 2023/04793-7. Surface photovoltage and photoelectrochemical measurements were supported by a grant from the U.S. Department of Energy, Office of Science, Office of Basic Energy Sciences under Award Number DOE-SC0015329.

**SUPPORTING INFORMATION**

Additional experimental details, transmittance and absorbance data, film thickness data, EDS maps and spectra, and light emission spectra.

## REFERENCES


(1) Walter, M. G.; Warren, E. L.; McKone, J. R.; Boettcher, S. W.; Mi, Q.; Santori, E. A.; Lewis, N. S. Solar Water Splitting Cells. *Chem Rev* **2010**, *110* (11), 6446–6473. https://doi.org/10.1021/cr1002326.

(2) Hu, S.; Shaner, M. R.; Beardslee, J. A.; Lichterman, M.; Brunschwig, B. S.; Lewis, N. S. Amorphous TiO2 Coatings Stabilize Si, GaAs, and GaP Photoanodes for Efficient Water Oxidation. *Science (1979)* **2014**, *344* (6187), 1005–1009. https://doi.org/10.1126/science.1251428.

(3) Suryawanshi, M. P.; Ghorpade, U. V.; Toe, C. Y.; Suryawanshi, U. P.; He, M.; Zhang, D.; Jang, J. S.; Shin, S. W.; Kim, J. H.; Hao, X.; Amal, R. Earth-Abundant Photoelectrodes for Water Splitting and Alternate Oxidation Reactions: Recent Advances and Future Perspectives. *Progress in Materials Science*. Elsevier Ltd April 1, 2023. https://doi.org/10.1016/j.pmatsci.2023.101073.

(4) Eftekhari, A.; Babu, V. J.; Ramakrishna, S. Photoelectrode Nanomaterials for Photoelectrochemical Water Splitting. *International Journal of Hydrogen Energy*. Elsevier Ltd April 20, 2017, pp 11078–11109. https://doi.org/10.1016/j.ijhydene.2017.03.029.

(5) Yang, W.; Prabhakar, R. R.; Tan, J.; Tilley, S. D.; Moon, J. Strategies for Enhancing the Photocurrent, Photovoltage, and Stability of Photoelectrodes for Photoelectrochemical Water Splitting. *Chemical Society Reviews*. Royal Society of Chemistry October 7, 2019, pp 4979–5015. https://doi.org/10.1039/c8cs00997j.

(6) Osterloh, F. E. Boosting the Efficiency of Suspended Photocatalysts for Overall Water Splitting. *Journal of Physical Chemistry Letters*. American Chemical Society August 7, 2014, pp 2510–2511. https://doi.org/10.1021/jz501342j.

(7) Raizada, P.; Sharma, S.; Kumar, A.; Singh, P.; Khan, A. A. P.; Asiri, A. M. Performance Improvement Strategies of CuWO4 Photocatalyst for Hydrogen Generation and Pollutant Degradation. *J Environ Chem Eng* **2020**, *8* (5), 104230. https://doi.org/10.1016/j.jece.2020.104230.

(8) Lalić, M. V.; Popović, Z. S.; Vukajlović, F. R. Electronic Structure and Optical Properties of CuWO4: An Ab Initio Study. *Comput Mater Sci* **2012**, *63*, 163–167. https://doi.org/10.1016/j.commatsci.2012.05.074.

(9) Tang, Y.; Rong, N.; Liu, F.; Chu, M.; Dong, H.; Zhang, Y.; Xiao, P. Enhancement of the Photoelectrochemical Performance of CuWO 4 Films for Water Splitting by Hydrogen Treatment. *Appl Surf Sci* **2016**, *361*, 133–140. https://doi.org/10.1016/j.apsusc.2015.11.129.

(10) Wu, Z.; Zhao, Z.; Cheung, G.; Doughty, R. M.; Ballestas-Barrientos, A. R.; Hirmez, B.; Han, R.; Maschmeyer, T.; Osterloh, F. E. Role of Surface States in Photocatalytic Oxygen

Evolution with CuWO 4 Particles . *J Electrochem Soc* **2019**, *166* (5), H3014–H3019. https://doi.org/10.1149/2.0021905jes.

(11) Yourey, J. E.; Pyper, K. J.; Kurtz, J. B.; Bartlett, B. M. Chemical Stability of CuWO4 for Photoelectrochemical Water Oxidation. *Journal of Physical Chemistry C* **2013**, *117* (17), 8708–8718. https://doi.org/10.1021/jp402048b.

(12) Lhermitte, C. R.; Bartlett, B. M. Advancing the Chemistry of CuWO4 for Photoelectrochemical Water Oxidation. *Acc Chem Res* **2016**, *49* (6), 1121–1129. https://doi.org/10.1021/acs.accounts.6b00045.

(13) Hao, Z.; Liu, Z.; Li, Y.; Ruan, M.; Guo, Z. Enhanced Photoelectrochemical Performance of 2D Core-Shell WO3/CuWO4 Uniform Heterojunction via in Situ Synthesis and Modification of Co-Pi Co-Catalyst. *Int J Hydrogen Energy* **2020**, *45* (33), 16550–16559. https://doi.org/10.1016/j.ijhydene.2020.04.135.

(14) Nam, K. M.; Cheon, E. A.; Shin, W. J.; Bard, A. J. Improved Photoelectrochemical Water Oxidation by the WO3/CuWO4 Composite with a Manganese Phosphate Electrocatalyst. *Langmuir* **2015**, *31* (39), 10897–10903. https://doi.org/10.1021/acs.langmuir.5b01780.

(15) Liu, Y.; Li, X.; Li, X.; Shao, C.; Han, C.; Xin, J.; Lu, D.; Niu, L.; Tang, Y.; Liu, Y. Highly Permeable WO3/CuWO4 Heterostructure with 3D Hierarchical Porous Structure for High-Sensitive Room-Temperature Visible-Light Driven Gas Sensor. *Sens Actuators B Chem* **2022**, *365*. https://doi.org/10.1016/j.snb.2022.131926.

(16) Wang, D.; Bassi, P. S.; Qi, H.; Zhao, X.; Gurudayal; Wong, L. H.; Xu, R.; Sritharan, T.; Chen, Z. Improved Charge Separation in WO3/CuWO4 Composite Photoanodes for Photoelectrochemical Water Oxidation. *Materials* **2016**, *9* (5), 348. https://doi.org/10.3390/ma9050348.

(17) Loka, C.; Gelija, D.; Vattikuti, S. V. P.; Lee, K. S. Silver-Boosted WO3/CuWO4 Heterojunction Thin Films for Enhanced Photoelectrochemical Water Splitting Efficiency. *ACS Sustain Chem Eng* **2023**, *11* (32), 11978–11990. https://doi.org/10.1021/acssuschemeng.3c02150.

(18) Rodríguez-Gutiérrez, I.; Djatoubai, E.; Rodríguez-Pérez, M.; Su, J.; Rodríguez-Gattorno, G.; Vayssieres, L.; Oskam, G. Photoelectrochemical Water Oxidation at FTO|WO 3 @CuWO 4 and FTO|WO 3 @CuWO 4 |BiVO 4 Heterojunction Systems: An IMPS Analysis. *Electrochim Acta* **2019**, *308*, 317–327. https://doi.org/10.1016/j.electacta.2019.04.030.

(19) Valenti, M.; Dolat, D.; Biskos, G.; Schmidt-Ott, A.; Smith, W. A. Enhancement of the Photoelectrochemical Performance of CuWO4 Thin Films for Solar Water Splitting by Plasmonic Nanoparticle Functionalization. *Journal of Physical Chemistry C* **2015**, *119* (4), 2096–2104. https://doi.org/10.1021/jp506349t.

(20) Gao, Y.; Zandi, O.; Hamann, T. W. Atomic Layer Stack Deposition-Annealing Synthesis of CuWO4. *J Mater Chem A Mater* **2016**, *4* (8), 2826–2830. https://doi.org/10.1039/c5ta06899a.

(21) Nomellini, C.; Polo, A.; Grigioni, I.; Marra, G.; Dozzi, M. V.; Selli, E. Ni(II)-Doped CuWO4 Photoanodes with Enhanced Photoelectrocatalytic Activity. *Photochemical and Photobiological Sciences* **2023**, *22* (12), 2759–2768. https://doi.org/10.1007/s43630-023-00484-4.

(22) Doughty, R. M.; Hodges, B.; Dominguez, J.; Han, R.; Zhao, Z.; Assavachin, S.; Osterloh, F. E. Fermi Level Pinning Controls Band Bending and Photochemical Charge Separation in Particles of N-SrTiO3, n-SrTiO3:Al, and n-GaAs:Te. *Journal of Physical Chemistry C* **2020**, *124* (34), 18426–18435. https://doi.org/10.1021/acs.jpcc.0c04989.

(23) Bard, A. J.; Bocarsly, A. B.; Fan, F.-R. F.; Walton, E. G.; Wrighton, M. S. The Concept of Fermi Level Pinning at Semiconductor/Liquid Junctions. Consequences for Energy Conversion Efficiency and Selection of Useful Solution Redox Couples in Solar Devices. *J Am Chem Soc* **1980**, *102* (11), 33–40.

(24) Hannula, M.; Ali-Löytty, H.; Lahtonen, K.; Sarlin, E.; Saari, J.; Valden, M. Improved Stability of Atomic Layer Deposited Amorphous TiO2 Photoelectrode Coatings by Thermally Induced Oxygen Defects. *Chemistry of Materials* **2018**, *30* (4), 1199–1208. https://doi.org/10.1021/acs.chemmater.7b02938.

(25) Moehl, T.; Suh, J.; Sévery, L.; Wick-Joliat, R.; Tilley, S. D. Investigation of (Leaky) ALD TiO2 Protection Layers for Water-Splitting Photoelectrodes. *ACS Appl Mater Interfaces* **2017**, *9* (50), 43614–43622. https://doi.org/10.1021/acsami.7b12564.

(26) Pham, H. H.; Wang, L. W. Oxygen Vacancy and Hole Conduction in Amorphous TiO2. *Physical Chemistry Chemical Physics* **2015**, *17* (1), 541–550. https://doi.org/10.1039/c4cp04209c.

(27) Ali-Löytty, H.; Hannula, M.; Saari, J.; Palmolahti, L.; Bhuskute, B. D.; Ulkuniemi, R.; Nyyssönen, T.; Lahtonen, K.; Valden, M. Diversity of TiO 2 : Controlling the Molecular and Electronic Structure of Atomic-Layer-Deposited Black TiO 2. *ACS Appl Mater Interfaces* **2019**, *11* (3), 2758–2762. https://doi.org/10.1021/acsami.8b20608.

(28) Shen, X.; Zhao, T.; Su, H.; Yang, M.; Chen, J.; Liu, Y.; Yanagi, R.; Solanki, D.; Hu, S. Tuning Intermediate Bands of Protective Coatings to Reach the Bulk-Recombination Limit of Stable Water-Oxidation GaP Photoanodes. *Adv Energy Mater* **2022**, *12* (29), 2201314. https://doi.org/10.1002/aenm.202201314.

(29) Guo, Z.; Ambrosio, F.; Pasquarello, A. Hole Diffusion across Leaky Amorphous TiO2 Coating Layers for Catalytic Water Splitting at Photoanodes. *J Mater Chem A Mater* **2018**, *6* (25), 11804–11810. https://doi.org/10.1039/c8ta02179a.

(30) Seo, S.; Shin, S.; Kim, E.; Jeong, S.; Park, N. G.; Shin, H. Amorphous TiO2Coatings Stabilize Perovskite Solar Cells. *ACS Energy Lett* **2021**, *6* (9), 3332–3341. https://doi.org/10.1021/acsenergylett.1c01446.

(31) Lichterman, M. F.; Carim, A. I.; McDowell, M. T.; Hu, S.; Gray, H. B.; Brunschwig, B. S.; Lewis, N. S. Stabilization of N-Cadmium Telluride Photoanodes for Water Oxidation to O2(g) in Aqueous Alkaline Electrolytes Using Amorphous TiO2 Films Formed by Atomic-Layer Deposition. *Energy Environ Sci* **2014**, *7* (10), 3334–3337. https://doi.org/10.1039/c4ee01914h.

(32) Lin, Y.; Battaglia, C.; Boccard, M.; Hettick, M.; Yu, Z.; Ballif, C.; Ager, J. W.; Javey, A. Amorphous Si Thin Film Based Photocathodes with High Photovoltage for Efficient Hydrogen Production. *Nano Lett* **2013**, *13* (11), 5615–5618. https://doi.org/10.1021/nl403265k.

(33) Bae, D.; Shayestehaminzadeh, S.; Thorsteinsson, E. B.; Pedersen, T.; Hansen, O.; Seger, B.; Vesborg, P. C. K.; Ólafsson, S.; Chorkendorff, I. Protection of Si Photocathode Using TiO2 Deposited by High Power Impulse Magnetron Sputtering for H2 Evolution in Alkaline Media. *Solar Energy Materials and Solar Cells* **2016**, *144*, 758–765. https://doi.org/10.1016/j.solmat.2015.10.020.

(34) Mei, B.; Pedersen, T.; Malacrida, P.; Bae, D.; Frydendal, R.; Hansen, O.; Vesborg, P. C. K.; Seger, B.; Chorkendorff, I. Crystalline TiO2: A Generic and Effective Electron-Conducting Protection Layer for Photoanodes and -Cathodes. *Journal of Physical Chemistry C* **2015**, *119* (27), 15019–15027. https://doi.org/10.1021/acs.jpcc.5b04407.

(35) Seger, B.; Pedersen, T.; Laursen, A. B.; Vesborg, P. C. K.; Hansen, O.; Chorkendorff, I. Using TiO2 as a Conductive Protective Layer for Photocathodic H2 Evolution. *J Am Chem Soc* **2013**, *135* (3), 1057–1064. https://doi.org/10.1021/ja309523t.

(36) Escaliante, L. C.; Pereira, A. L. de J.; Affonço, L. J.; da Silva, J. H. D. Multilayered TiO2/TiO2−x/TiO2 Films Deposited by Reactive Sputtering for Photocatalytic Applications. *J Mater Res* **2021**, 36, 3096–3108. https://doi.org/10.1557/s43578-021-00310-6.

(37) Cisneros, J. I. Optical Characterization of Dielectric and Semiconductor Thin Films by Use of Transmission Data. *Appl Opt* **1998**, *37*, 5262–5270. https://doi.org/10.1364/AO.37.005262.

(38) Souza, E. L. S.; Sczancoski, J. C.; Nogueira, I. C.; Almeida, M. A. P.; Orlandi, M. O.; Li, M. S.; Luz, R. A. S.; Filho, M. G. R.; Longo, E.; Cavalcante, L. S. Structural Evolution, Growth Mechanism and Photoluminescence Properties of CuWO4 Nanocrystals. *Ultrason Sonochem* **2017**, *38*, 256–270. https://doi.org/10.1016/j.ultsonch.2017.03.007.

(39) Ruiz-Fuertes, J.; Sanz-Ortiz, N.; Gonzlez, J.; Rodríguez, F.; Segura, A.; Errandonea, D. Optical Absorption and Raman Spectroscopy of CuWO4. In *Solid State Communications*; 1974; Vol. 215. https://doi.org/10.1088/1742-6596/215/1/012048.

(40) Ruiz-Fuertes, J.; Errandonea, D.; Segura, A.; Manjon, F. J.; Zhu, Z.; Tu, C. Y. Growth, Characterization, and High-Pressure Optical Studies of CuWO 4. In *High Pressure Research*; 2008; Vol. 28, pp 565–570. https://doi.org/10.1080/08957950802446643.

(41) Daniel, M. F.; Lassegues, J. C.; Gerand, B.; Fjglarz, M. *Infrared and Raman Study of W03 Tungsten Trioxides and W03, XHzO Tungsten Trioxide Hydrates*; 1987; Vol. 67.

(42) Boulova, M.; Lucazeau, G. Crystallite Nanosize Effect on the Structural Transitions of WO3 Studied by Raman Spectroscopy. *J Solid State Chem* **2002**, *167* (2), 425–434. https://doi.org/10.1006/jssc.2002.9649.

(43) Halliday, D.; Walker, J.; Resnick, R. *Fundamentals of Physics*, 8th ed.; John Wiley & Sons, Inc: New York, 2007.

(44) Pankove, J. I. *Optical Processes in Semiconductors*; Dover Publications, Inc: New York, 1971.

(45) Fox, M. *Optical Properties of Solids*, 2nd ed.; Oxford University Press, 2010.

(46) Fowles, G. R. *Introduction to Modern Optics*, 2nd ed.; Dover Publications, Inc.: New York, 1989.

(47) Zhao, J.; Osterloh, F. E. Photochemical Charge Separation in Nanocrystal Photocatalyst Films: Insights from Surface Photovoltage Spectroscopy. *Journal of Physical Chemistry Letters* **2014**, *5* (5), 782–786. https://doi.org/10.1021/jz500136h.

(48) Frame, F. A.; Townsend, T. K.; Chamousis, R. L.; Sabio, E. M.; Dittrich, T.; Browning, N. D.; Osterloh, F. E. Photocatalytic Water Oxidation with Nonsensitized IrO2 Nanocrystals under Visible and UV Light. *J Am Chem Soc* **2011**, *133* (19), 7264–7267. https://doi.org/10.1021/ja200144w.

(49) Waller, M. R.; Townsend, T. K.; Zhao, J.; Sabio, E. M.; Chamousis, R. L.; Browning, N. D.; Osterloh, F. E. Single-Crystal Tungsten Oxide Nanosheets: Photochemical Water Oxidation in the Quantum Confinement Regime. *Chemistry of Materials* **2012**, *24* (4), 698–704. https://doi.org/10.1021/cm203293j.

(50) Daemi, S.; Kundmann, A.; Becker, K.; Cendula, P.; Osterloh, F. E. Contactless Measurement of the Photovoltage in BiVO4 Photoelectrodes. *Energy Environ Sci* **2023**, *16* (10), 4530–4538. https://doi.org/10.1039/d3ee02087h.

(51) Daemi, S.; Kaushik, S.; Das, S.; Hamann, T. W.; Osterloh, F. E. BiVO4-Liquid Junction Photovoltaic Cell with 0.2% Solar Energy Conversion Efficiency. *J Am Chem Soc* **2023**, *145* (47), 25797–25805. https://doi.org/10.1021/jacs.3c09546.

(52) Cheng, Y.; Xiao, C.; Mahmoudi, B.; Scheer, R.; Maijenburg, A. W.; Osterloh, F. E. Effect of Charge Selective Contacts on the Quasi Fermi Level Splitting of CuGa 3 Se 5 Thin Film Photocathodes for Hydrogen Evolution and Methylviologen Reduction . *EES Catalysis* **2023**, *1* (1), 74–83. https://doi.org/10.1039/d2ey00062h.

(53) Doughty, R. M.; Chowdhury, F. A.; Mi, Z.; Osterloh, F. E. Surface Photovoltage Spectroscopy Observes Junctions and Carrier Separation in Gallium Nitride Nanowire Arrays for Overall Water-Splitting. *Journal of Chemical Physics* **2020**, *153* (14), 144707. https://doi.org/10.1063/5.0021273.

(54) Pyper, K. J.; Yourey, J. E.; Bartlett, B. M. Reactivity of CuWO4 in Photoelectrochemical Water Oxidation Is Dictated by a Midgap Electronic State. *Journal of Physical Chemistry C* **2013**, *117* (47), 24726–24732. https://doi.org/10.1021/jp408434v.

(55) Wang, D.; Bassi, P. S.; Qi, H.; Zhao, X.; Gurudayal; Wong, L. H.; Xu, R.; Sritharan, T.; Chen, Z. Improved Charge Separation in WO3/CuWO4 Composite Photoanodes for Photoelectrochemical Water Oxidation. *Materials* **2016**, *9* (5), 348. https://doi.org/10.3390/ma9050348.

(56) Chen, Z.; Yao, D.; Chu, C.; Mao, S. Photocatalytic H2O2 Production Systems: Design Strategies and Environmental Applications. *Chemical Engineering Journal*. Elsevier B.V. January 1, 2023. https://doi.org/10.1016/j.cej.2022.138489.

(57) Tsukamoto, D.; Shiro, A.; Shiraishi, Y.; Sugano, Y.; Ichikawa, S.; Tanaka, S.; Hirai, T. Photocatalytic H 2O 2 Production from Ethanol/O 2 System Using TiO 2 Loaded with Au-Ag Bimetallic Alloy Nanoparticles. *ACS Catal* **2012**, *2* (4), 599–603. https://doi.org/10.1021/cs2006873.

(58) Teranishi, M.; Naya, S. I.; Tada, H. In Situ Liquid Phase Synthesis of Hydrogen Peroxide from Molecular Oxygen Using Gold Nanoparticle-Loaded Titanium(IV) Dioxide Photocatalyst. *J Am Chem Soc* **2010**, *132* (23), 7850–7851. https://doi.org/10.1021/ja102651g.

**Table Of Contents (TOC)**